White Rose Research Online

eprints@whiterose.ac.uk
https://eprints.whiterose.ac.uk
Universities of Leeds, Sheffield and York

Deposited via The University of Sheffield.

White Rose Research Online URL for this paper:
https://eprints.whiterose.ac.uk/id/eprint/169794/

Version: Published Version

Article:
Gillard, D.J., Genco, A., Ahn, S. et al. (2021) Strong exciton-photon coupling in large area MoSe2 and WSe2 heterostructures fabricated from two-dimensional materials grown by chemical vapor deposition. 2D Materials, 8 (1). 011002. ISSN: 2053-1583

https://doi.org/10.1088/2053-1583/abc5a1

Reuse
This article is distributed under the terms of the Creative Commons Attribution (CC BY) licence. This licence allows you to distribute, remix, tweak, and build upon the work, even commercially, as long as you credit the authors for the original work. More information and the full terms of the licence here: https://creativecommons.org/licenses/

Takedown
If you consider content in White Rose Research Online to be in breach of UK law, please notify us by emailing eprints@whiterose.ac.uk including the URL of the record and the reason for the withdrawal request.

UNIVERSITY OF LEEDS
University of Sheffield
UNIVERSITY of York

2D Materials

LETTER • **OPEN ACCESS**

Strong exciton-photon coupling in large area $MoSe_2$ and WSe_2 heterostructures fabricated from two-dimensional materials grown by chemical vapor deposition

To cite this article: Daniel J Gillard *et al* 2021 *2D Mater.* **8** 011002

View the article online for updates and enhancements.

This content was downloaded from IP address 46.64.192.19 on 01/02/2021 at 15:38

2D Materials

LETTER

Strong exciton-photon coupling in large area $MoSe_2$ and WSe_2 heterostructures fabricated from two-dimensional materials grown by chemical vapor deposition

Daniel J Gillard[1], Armando Genco[1], Seongjoon Ahn[2], Thomas P Lyons[1], Kyung Yeol Ma[2], A-Rang Jang[2], Toby Severs Millard[1], Aurélien A P Trichet[3], Rahul Jayaprakash[1], Kyriacos Georgiou[1], David G Lidzey[1], Jason M Smith[3], Hyeon Suk Shin[2] and Alexander I Tartakovskii[1]

[1] Department of Physics and Astronomy, University of Sheffield, Sheffield S3 7RH, United Kingdom
[2] Department of Energy Engineering, Department of Chemistry, and Low Dimensional Carbon and 2D Materials Center, Ulsan National Institute of Science and Technology, Ulsan 44919, Republic of Korea
[3] Department of Materials, University of Oxford, Parks Road, Oxford OX1 3PH, United Kingdom

E-mail: a.genco@sheffield.ac.uk **and** a.tartakovskii@sheffield.ac.uk

Keywords: transition metal dichalcogenides, optical microcavity, strong light–matter interaction, hexagonal boron nitride, chemical vapour deposition, van der Waals heterostructures

Supplementary material for this article is available online

OPEN ACCESS

RECEIVED
7 September 2020

REVISED
20 October 2020

ACCEPTED FOR PUBLICATION
28 October 2020

PUBLISHED
18 November 2020

Original Content from this work may be used under the terms of the Creative Commons Attribution 4.0 licence.

Any further distribution of this work must maintain attribution to the author(s) and the title of the work, journal citation and DOI.

Abstract

Two-dimensional semiconducting transition metal dichalcogenides embedded in optical microcavities in the strong exciton-photon coupling regime may lead to promising applications in spin and valley addressable polaritonic logic gates and circuits. One significant obstacle for their realization is the inherent lack of scalability associated with the mechanical exfoliation commonly used for fabrication of two-dimensional materials and their heterostructures. Chemical vapor deposition offers an alternative scalable fabrication method for both monolayer semiconductors and other two-dimensional materials, such as hexagonal boron nitride. Observation of the strong light-matter coupling in chemical vapor grown transition metal dichalcogenides has been demonstrated so far in a handful of experiments with monolayer molybdenum disulfide and tungsten disulfide. Here we instead demonstrate the strong exciton-photon coupling in microcavities composed of large area transition metal dichalcogenide/hexagonal boron nitride heterostructures made from chemical vapor deposition grown molybdenum diselenide and tungsten diselenide encapsulated on one or both sides in continuous few-layer boron nitride films also grown by chemical vapor deposition. These transition metal dichalcogenide/hexagonal boron nitride heterostructures show high optical quality comparable with mechanically exfoliated samples, allowing operation in the strong coupling regime in a wide range of temperatures down to 4 Kelvin in tunable and monolithic microcavities, and demonstrating the possibility to successfully develop large area transition metal dichalcogenide based polariton devices.

1. Introduction

Monolayers of transition metal dichalcogenides (TMDs) are promising semiconductors with unique electrical and optical properties arising from the quantum confinement experienced by the electrons and holes in the two-dimensional (2D) structure [1, 2]. One of the main effects is the appearance of direct bandgap excitonic transitions showing features strongly beneficial for optoelectronics, such as high binding energies and very large oscillator strengths [3, 4]. Moreover, the breaking of spatial inversion symmetry in the 2D lattice and a large spin–orbit coupling generate spin-valley locked optically addressable excitons at the K and K′ points of the momentum space [3, 5]. These exceptional properties can be further enriched by integrating the TMDs within optical resonators enabling the strong exciton-photon coupling regime, where confined photons and excitons hybridize into new states called polaritons [6–12]. Polaritons in TMDs acquire novel properties arising from the valley pseudo-spin degree of freedom

© 2020 The Author(s). Published by IOP Publishing Ltd

of excitons [13, 14], and further provide enhanced valley coherence for excitons strongly coupled with long-lived cavity photons [15, 16]. Efficient polariton propagation in TMDs has been recently observed, with diffusion lengths of up to 20 μm in WS_2 at room temperature [17], while valley-dependent divergent polariton diffusion has been found in $MoSe_2$ at cryogenic temperatures, whereby polaritons spread in different in-plane directions owing to the exciton valley Hall effect [18]. Polaritons in TMDs already offer the potential to create highly non-linear phenomena [7, 19, 20], with further effort directed at realization of Bose–Einstein condensation [19, 21], polariton lasing [22, 23] and optical parametric oscillation [24] so far observed in other material systems. United to the valley degree of freedom of TMD monolayers, these phenomena could be exploited to create large scale all-optical polariton circuits and quantum networks [25, 26].

However, TMD monolayers are usually fabricated by mechanical exfoliation, resulting in high quality but small sized flakes, hindering the reproducibility and scalability of the devices. Chemical vapor deposition (CVD) offers an alternative growth and fabrication method that provides substrate-wide coverage of uniform monolayer islands [27], as well as the ability to grow heterostructures in-situ [28], therefore completely bypassing the mechanical transfers necessary in exfoliated equivalents and minimizing external contamination. CVD provides a very attractive and scalable method for the fabrication of large scale TMD based devices. As such, CVD-grown MoS_2 and WS_2 flakes have already been employed in polaritonic devices working at room temperature [6, 29]. Nevertheless, in order to enhance the polariton valley properties and optimize coherence, narrow exciton linewidths (low inhomogeneous broadening) and low structural disorder are needed, which up to now have only been shown by exfoliated $MoSe_2$ and WSe_2 monolayers at low temperatures [7–11, 13, 15]. Another advantage of high quality structures combined with the possibility to operate at low temperature will be access to highly non-linear trion-polaritons [7, 20] or Fermi-polaron-polaritons [9], requiring control and stability of the charged excitons, as well as employment of suitable heterostructures [9] composed of TMDs, hexagonal boron nitride (hBN) and graphene.

Here, we show large area $MoSe_2$ and WSe_2 monolayers encapsulated in hBN, all grown by CVD, with crystal domains exceeding 100 μm in size, which display high optical quality, rivaling exfoliated material. This is evidenced by the intense and narrow exciton peaks observed in photoluminescence (PL) measurements and in reflectance contrast (RC). Substrate-wide growth uniformity and a high degree of alignment within the ensemble of monolayer domains has been achieved in these materials using CVD growth on sapphire for $MoSe_2$ and directly on CVD-synthesized hBN for WSe_2. We have confirmed these favorable monolayer TMD crystal properties by using a recently developed substrate-wide statistical analysis of TMD crystal axes orientation and PL properties [30]. Further testing of the samples in a tunable microcavity exposes clear evidence of strong exciton-photon coupling and formation of exciton-polariton states. An anti-crossing is observed between the cavity mode and neutral exciton transition, with Rabi splittings of 17 meV for both $MoSe_2$ and WSe_2, very similar in magnitude with exfoliated materials [8, 9, 13, 15], highlighting similar optical qualities. Finally, as a proof of concept for future large scale TMD-based polaritonic devices, a monolithic SiO_2 cavity is fabricated incorporating CVD grown hBN-encapsulated $MoSe_2$, in which strong coupling is observed with a large Rabi splitting of 34 meV at $T = 4$ K and 31 meV at $T = 150$ K. The results presented in this work demonstrate the possibility to fabricate large area polariton devices exploiting high quality TMD based heterostructures made from CVD-grown materials, paving the way for future scalable TMD-polaritonic circuits.

2. Results and discussion

Two types of encapsulated heterostructure (HS) have been fabricated from CVD-grown materials for this work (see further details in Methods). In the first heterostructure, HS1 (figure 1(a)), $MoSe_2$ monolayers are grown by CVD onto a sapphire substrate. Thousands of individual monolayer islands, positioned throughout the entire substrate, are then mechanically transferred using a polystyrene membrane onto a high reflectivity distributed Bragg reflector (DBR) composed of 13 pairs of SiO_2/Ta_2O_5 with the high reflectance stop-band centered at a wavelength of 750 nm. A substrate-wide few-layer film of hexagonal boron nitride (hBN), also grown by CVD, is mechanically transferred on top of the $MoSe_2$ flakes to complete the encapsulation. For the second heterostructure, HS2 (figure 1(b)), WSe_2 monolayers are grown by CVD directly on few-layer hBN, also grown by CVD. Both materials, WSe_2/hBN, are then mechanically transferred, at once, onto the DBR and subsequently encapsulated with a few-layer film of CVD grown hBN. It has been shown that for mechanically exfoliated TMDs, an encapsulation with thin hBN provides uniform dielectric screening of the Coulomb interaction, reducing spatial inhomogeneity in the exciton, thereby narrowing the emission linewidth [27, 31]. Furthermore, hBN protects the TMD layers in the heterostructure from damage and contamination during the subsequent deposition of various dielectrics in microcavity structures relevant to our work [32]. Moreover, the direct growth of TMD monolayers on hBN is also strongly beneficial

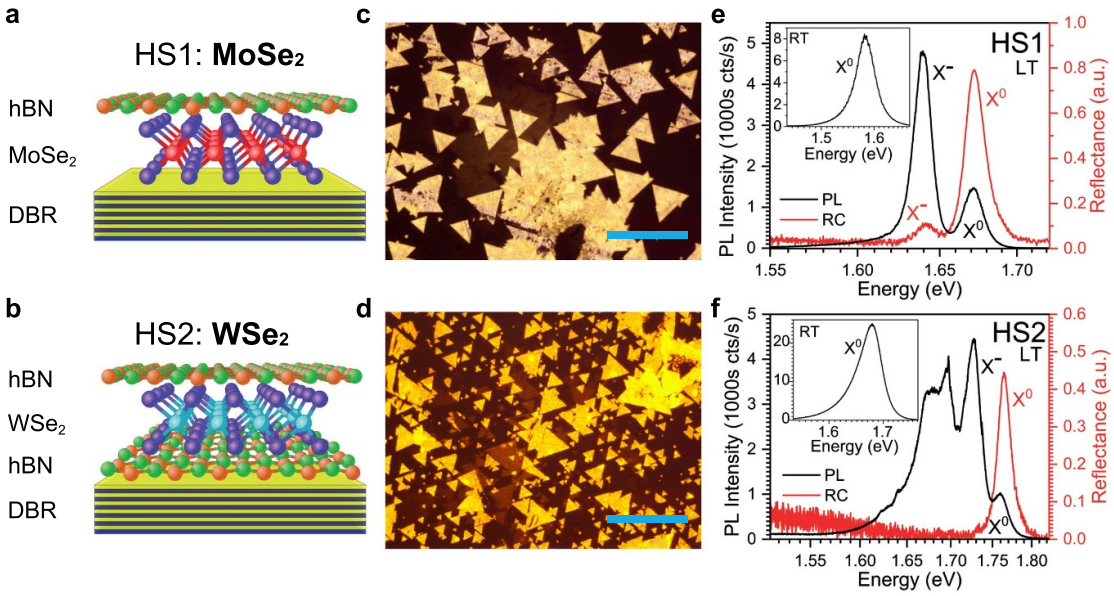

Figure 1. (a), (b) Schematics of the CVD grown heterostructures (not to scale). (a) HS1: $MoSe_2$ monolayers are grown by CVD on a sapphire substrate, mechanically transferred onto a DBR mirror and encapsulated with hBN. (b) HS2: WSe_2 monolayers are grown by CVD on multilayer hBN, transferred together with the hBN onto a DBR mirror and encapsulated with multilayer hBN. The hBN multilayers are also grown by CVD. (c), (d) Optical microscope images of the photoluminescence (PL) from (c) HS1 and (d) HS2 taken at room temperature using a 50x objective lens (scale bar: 50 μm). (e), (f) Optical characterization of (e) HS1 and (f) HS2 at T ~4 K. Insets show PL spectra at room temperature. PL and reflectance contrast (RC) spectra are shown in black and red, respectively. At low T, both samples show emission from both neutral, X^0, and charged, X^-, excitons, whereas only HS1 shows absorption from both. PL cw excitation conditions: $\lambda_{exc} = 660$ nm, P = 20 μW for HS1; $\lambda_{exc} = 532$ nm, P = 20 μW for HS2.

as a route to single-crystal epitaxial growth [30, 33], which, up until now, has been demonstrated with a limited range of TMD materials such as WS_2 [34] and MoS_2 [35]. Fully coalesced CVD grown WSe_2 monolayer films were obtained very recently by Zhang *et al* [33], through a careful control of nucleation and extended lateral growth time, and a strong improvement of optical and electrical properties have been achieved compared to the same material grown on sapphire.

As a first characterization step, the room temperature PL emission and the general morphology of the structures have been analyzed under an optical microscope (see Methods). HS1 (figure 1(c)) generally consists of large isolated monolayer islands with characteristic triangular shape and average lateral size of 8 μm (see Supplementary Note I (stacks.iop.org/TDM/08/011002/mmedia) for details), along with a number of regions where multiple flakes merge to form monolayers with sizes exceeding 100 μm. Similarly, HS2 (figure 1(d)) shows large triangular monolayer flakes with average lateral widths of 11 μm. Again, in areas where flakes merge, monolayers of over 100 μm in width can be seen. Large areas of uniform coverage are necessary for constructing large arrays of identical heterostructure devices, such as transistors or photodetectors. Overall, there is monolayer coverage of 14% (1.75 mm^2) for HS1 and 22% (3.67 mm^2) for HS2, calculated by dividing the total area of monolayer across the sample by the total substrate area. The substrate-scale PL imaging analysis [30] used to identify the monolayers is discussed in more detail below.

Further optical characterization of the two heterostructures has been performed using a spectroscopic microscopy setup at both room (~290 K) and low (~4 K) temperature (figures 1(e) and (f)). PL measurements are carried out by exciting the samples with an off resonant continuous wave (cw) laser at a power of 20 μW (see Methods). The considerable room temperature excitonic PL emission shown in the insets in figures 1(e), (f) highlights the large exciton binding energy associated with TMD monolayers [4]. In HS1 the exciton PL peak is located at 1.579 eV with a linewidth of 40 meV, and HS2 displays the exciton peak at 1.670 eV with a similar linewidth of 45 meV, typical of $MoSe_2$ and WSe_2 monolayers operating at room temperatures.

Decreasing the temperature to ~4 K produces a narrowed and blue shifted neutral exciton PL peak, X^0, at 1.671 eV in HS1 and 1.759 eV in HS2, and a second peak attributed to the charged exciton (trion) transition, X^-, which appears at 1.639 eV in HS1 and 1.726 eV in HS2, about 30 meV below the neutral exciton [8, 13, 36]. The relative intensity of the X^- peak, when compared to the X^0 peak, is heavily influenced by the free carrier densities present in the structures [3]. In HS2, PL seen at lower energies (below 1.70 eV) has previously been attributed to various excitonic complexes in WSe_2 including spin dark excitons [37], exciton-phonon side-bands [38] and localized states [39]. The samples show neutral

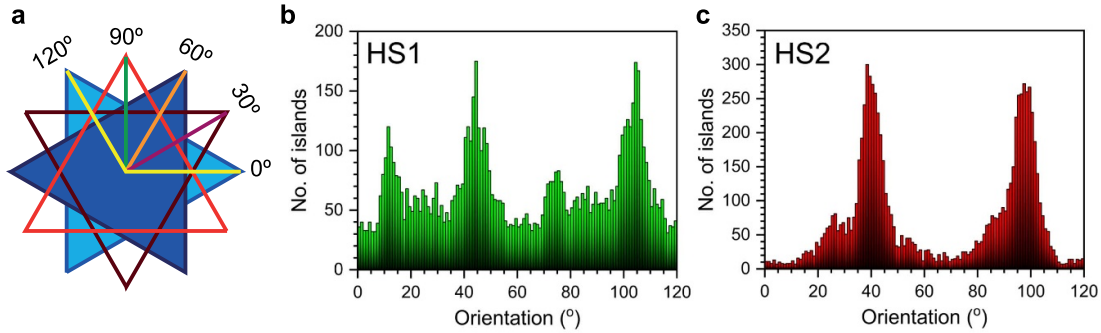

Figure 2. (a) Schematic showing flake orientations at different angles relative to the horizontal axis of the microscope images. (b), (c) Analysis of flake orientation. Islands of monolayer TMD are identified and the orientation extracted using methodology as described in previous investigations [30]. Both (b) HS1 and (c) HS2 show two main peaks situated 60° apart, while HS1 also shows two extra peaks situated at 30° from the main peaks.

exciton linewidths of 13 meV and 21 meV for HS1 and HS2 respectively, and 12 meV and 20 meV for the charged exciton of the two samples. Generally, the linewidth of an excitonic transition in TMD monolayers is strongly affected by the level of structural disorder and density of defects [29]. The spectral shapes and linewidths demonstrated by the CVD grown samples investigated in this work improve upon those reported by Zhang *et al* [33] and Lippert *et al* [40], and are similar to exfoliated flakes operating at low temperature without encapsulation (see Supplementary Note IV) [8, 15, 27, 31, 36]. This shows that CVD growth can produce heterostructures of comparable optical quality to mechanically exfoliated flakes. The role of hBN is mostly to provide a high quality substrate for the TMD synthesis [30, 33], but also to act as a buffer layer protecting TMDs from damage during the deposition of additional layers in order to complete a microcavity or waveguide structure.

We also measure reflectance contrast spectra using a broad band white light source and calculated as $\Delta R/R = (R_{sub} - R_{HS})/R_{sub}$, where R_{HS} is the reflectance of the heterostructure, and R_{sub} is the reflectance of the bare substrate in between the TMD flakes. These spectra (red lines in figures 1(e), (f)) reveal a strong absorption peak attributed to the X^0 transition in both heterostructures and a lower intensity peak at lower energy attributed to X^- in HS1. The relative peak height is strictly related to the oscillator strength of individual transitions, with the neutral exciton being much more intense than the trion in HS1 due to a relatively low doping level. The X^0 absorption peak of HS2 is slightly broader than in HS1, similar to the trend observed for the PL spectra, which is an indication of the greater structural disorder present in CVD-grown WSe_2.

As can be inferred in figures 1(c) and (d), the bright triangular monolayer islands appear to have a preferred orientation. To extract the size and shape of monolayer flakes, shape recognition techniques were used on a full substrate map comprised of multiple microscope PL images, an example of one such image is shown in figures 1(c) and (d). By employing analytical methods detailed in our previous work [30], the flake orientation relative to the horizontal axis of the microscope image can be found. In order to maximize accuracy, only islands with shape close to equilateral triangles are analyzed in terms of angular orientation. Of the 16 999 (14 205) individual monolayer islands identified in HS1 (HS2), 8089 (8391) satisfy this condition. Measured in terms of area, this corresponds to 21% (17%) of the total monolayer coverage. The histograms in figures 2(b) and (c) detail the number of islands identified as a function of orientation angle, showing that both the samples feature a very high degree of island orientation uniformity, a signature of epitaxial growth. For WSe_2 grown directly onto hBN (figure 2(c)), two main orientations have been found, 60° apart. This is expected from equilateral triangular islands growing in two preferential directions at 60° relative to one another. These two preferential directions are directly related to the hexagonal crystal structure of the growth substrate and have also been observed in previous studies of MoS_2, WS_2, and WSe_2 grown by CVD on hBN [30, 33–35]. For $MoSe_2$ grown onto c-plane sapphire (figure 2(b)), four peaks in the angular distribution are observed. Two main peaks show the preferred flake orientation, situated at 60° relative to each other, along with two less populated angles at 30° relative to the two main peaks. Both two, and four preferential growth directions have been seen in TMDs grown via CVD onto c-plane sapphire [41, 42]. Control over the relative angle of the flakes at the synthesis stage of fabrication will provide the basis to build scalable heterostructures with control over the relative interlayer crystallographic orientation.

After the optical characterization step, the encapsulated heterostructures are tested in a tunable open cavity setup which consists of a top concave DBR mirror distanced 2–3 μm from a planar bottom DBR mirror (figures 3(a) and (b)), upon which the HSs

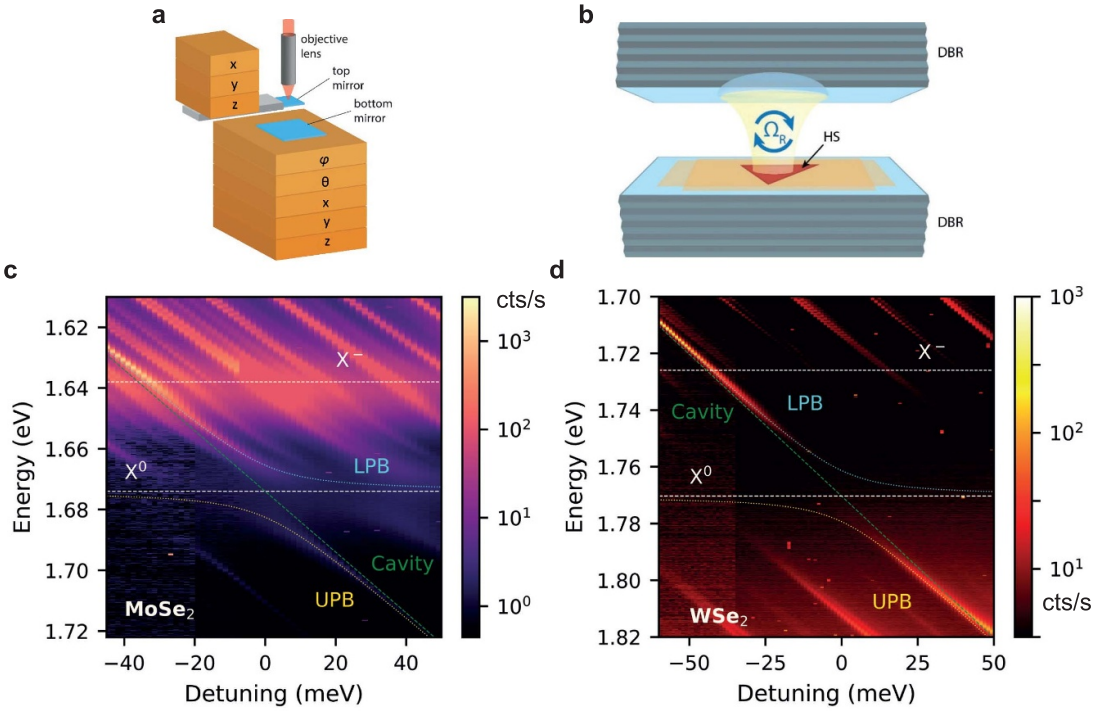

Figure 3. (a) Schematic of the tunable open microcavity including the set of piezo actuators used to align the mirrors and perform the PL scans of the heterostructure. (b) Schematic of the optical microcavity. The cavity is composed of a planar DBR, upon which the HS is placed, and a concave top DBR confining the optical cavity mode in 3 dimensions. (c), (d) PL emission from (c) HS1 and (d) HS2 displayed as a function of photon energy and exciton-photon detuning ($\Delta = E_c - E_{X^0}$). Clear anti-crossings of the cavity mode with the exciton are observed in both heterostructures. PL spectra are fitted using a Lorentzian peak (see Supplementary Note II) and a two level coupled oscillator model is used to extract the lower (blue curve) and upper (yellow curve) polariton branches, excitonic resonances (white horizontal lines), and LG_{00} photonic mode (green diagonal line). Rabi splittings of 17 meV are found for both HS1 and HS2. Samples are optically excited using a 637 nm cw laser.

are placed [8, 9, 13, 15, 43]. The mirrors are positioned using piezo-actuator stages (figure 3(a)). Free space optical access from above the top concave DBR allows laser excitation and optical detection, using an achromatic doublet objective lens. The cavity length can be tuned by slowly moving the bottom mirror along the z-axis, thus allowing the tuning of the cavity mode (diagonal green dashed lines in figures 3(c), (d)). The PL signal collected from the TMDs, as the cavity length is reduced, is displayed in figures 3(c) and (d) as a function of detuning (the energy difference between the cavity mode and unperturbed exciton, X^0). The three dimensional optical confinement provided by the concave top mirror generates a set of transverse modes for each longitudinal mode [8, 43] also visible in both figures.

When the fundamental longitudinal cavity mode, LG_{00} (green diagonal dashed lines in figures 3(c) and (d)) which ensures the highest light confinement, is tuned into resonance with the exciton transition energies, light matter coupling can manifest in one of two ways, both of which are observed in HS1 (figure 3(c)). As the cavity mode is tuned into resonance with the trion, X^-, at 1.638 eV, the cavity mode is broadened and brightened, a demonstration of the weak coupling [8, 13, 15, 44] arising from the reduced oscillator strength of the trion transition. The absence of mode broadening in HS2 (figure 3(d)) cavity scans at the trion energy is an indication that the absorption of the WSe_2 trion resonance, occurring in HS2 at 1.726 eV, is too weak, as also confirmed in figure 1(f).

The second regime of exciton-photon coupling, known as the strong coupling, presents itself as an anti-crossing of the LG_{00} cavity mode and the exciton energies with a characteristic Rabi splitting, $2\hbar\Omega_R$, at the resonance. This behavior can be clearly observed in both HS1 (figure 3(c)) and HS2 (figure 3(d)) as the LG_{00} is tuned into resonance with the neutral exciton, at 1.673 eV for HS1 and 1.770 eV for HS2. The peak positions of the lower (LPB) and upper (UPB) polariton branches have been extracted using a Lorentzian peak fitting, and used to fit a two-level coupled oscillator model (detailed in Supplementary Note II) in order to determine $2\hbar\Omega_R$ as shown overlaid in figures 3(c), (d). We find a value of 17.2 $\pm$ 3.3 meV for HS1 and 16.8 $\pm$ 3.1 meV for HS2.

These measurements demonstrate large Rabi splittings closely comparable to the values observed in exfoliated monolayer $MoSe_2$ and WSe_2 placed in zero-dimensional tunable microcavities [9, 13, 15, 43]. This further confirms, thanks to the

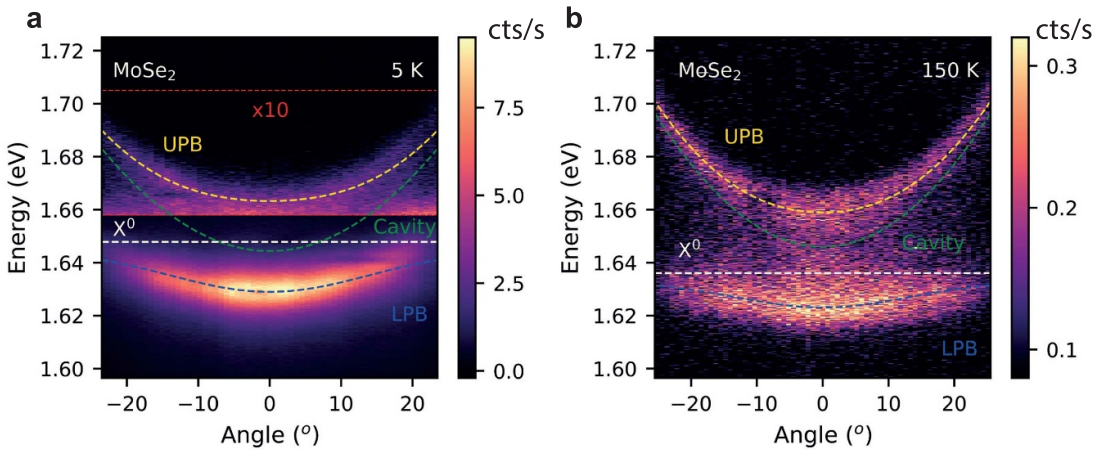

Figure 4. (a), (b) Angle resolved PL imaging of HS1 monolithic cavity. (a) At 5 K, the cavity has a negative detuning at 0° of $\Delta \approx -3.5$ meV, showing anti-crossings at $\pm 7^{\circ}$. The PL intensity in the region within the red dashed lines has been multiplied by a factor of 10 for clarity. (b) At 150 K, the cavity has a positive detuning at 0° of $\Delta \approx 10$ meV. We overlay the fitted LPB (blue) and UPB (yellow) along with the extracted parabolic cavity dispersion (green) and neutral exciton resonance (white). A Rabi splitting of 34 ± 4 meV and 31 ± 4 meV is observed at 5 K and 150 K, respectively. The sample is optically excited using a 660 nm cw laser at a power of 50 μW.

reduced structural disorder in the presented heterostructures, the high optical quality of the hBN encapsulated CVD grown TMD monolayers, hence proving the validity for CVD growth techniques when designing scalable devices.

Further advantages of large area TMDs can be exploited in monolithic cavities, providing a platform to form various topological designs to adapt or enhance device functionality towards polariton circuits [25, 26]. For these devices, the protective function of the hBN encapsulation is of particular importance as the top dielectric mirror needs to be deposited on top of the TMD layers [32]. As a proof of concept, we deposited 98 nm of SiO_2 via e-beam deposition, followed by a semi-transparent layer of 50 nm gold, on top of HS1 to fabricate a $\lambda/2$ monolithic cavity (see Supplementary Note III). The oxide deposition process has been carried out at room temperature in order to preserve the optical integrity of the emitting materials as much as possible [32, 45].

In the tunable cavity, the photonic modes are confined in all three dimensions, resulting in a set of discrete cavity modes, with $k_{x,y,z} \sim 0$, which are tuned in energy by altering the cavity length. By contrast, in a monolithic two-dimensional cavity, as in our case, the photonic mode is confined only in the vertical z direction, and thus a cavity mode energy dispersion as a function of continuous $k_{x,y}$ values is observed [44]. This dispersion can be probed by measuring angle-resolved PL or reflectivity spectra as a function of angle measured from the normal to the sample (corresponding to $k_{x,y} = 0$)[44]. In the cavity used in our experiment, a stronger light confinement can be achieved than in the tunable devices presented earlier, due to a smaller vertical size of the cavity and lower mode penetration into the mirrors. As shown below, this leads to a higher magnitude of the Rabi splitting. Since monolithic cavities are not tunable in size, the temperature dependence of the X^0 transition energy (further discussed in Supplementary Note III) is used to tune the exciton into resonance with the photonic mode which has a negligible dependence of its frequency with temperature.

The PL collected from the monolithic cavity while being optically excited by non-resonant continuous wave laser in the linear power regime, as imaged by angle resolved spectroscopy probing the exciton and photon states at different k-vectors, is shown in figure 4. In figure 4(a) at a temperature of 5 K, the X^0 transition is at 1.648 eV, while in figure 4(b) at 150 K, the X^0 red-shifts to 1.636 eV. The monolithic cavity shows strong exciton-photon coupling signatures in PL at both the temperatures, owing to the protective capability of the CVD grown hBN which helped shield the $MoSe_2$ monolayers from the potentially damaging SiO_2 deposition process.

At a temperature of 5 K, the exciton is negatively detuned from the cavity mode at 0° by - 3.5 meV, such that the LPB is much more visible than the UPB. To show the upper polariton branch in figure 4(a) the collected intensity values have been multiplied by a factor of 10 between 1.658 and 1.705 eV, as outlined by red dashed lines. By fitting the PL emission spectra with Lorentzian peaks and applying the extracted peak positions to a two level coupled-oscillator model (see Supplementary Note II) [44] we obtain a large Rabi splitting of 34.1 ± 4.0 meV at 5 K. The exciton-photon coupling strength in the monolithic cavity is higher than in the open cavity due to the increased light confinement. The two

polariton branches, cavity dispersion, and exciton energy obtained from the coupled-oscillator model are shown overlaying figures 4(a) and (b), with an anti-crossing clearly seen at $\pm 7^{\circ}$ when the device is at 5 K. The strongly coupled cavity performs well up to 150 K, when the excitonic mode is positively detuned ($\Delta(0^{o}) = +10$ meV), leading to a Rabi splitting of 30.5 ± 3.9 meV.

3. Conclusion

In summary, high quality substrate-wide $MoSe_2$, and WSe_2, TMD monolayers encapsulated with large area hBN were fabricated using CVD growth techniques, and subsequently embedded in tunable and monolithic microcavity devices where strong exciton-photon coupling was observed. The heterostructures show optical properties comparable with exfoliated materials, and consequently exhibit similar values of polariton Rabi splittings to previously studied heterostructures made from exfoliated flakes [8, 9, 13, 15].

Furthermore, the demonstrated CVD growth on sapphire and hBN produced highly orientated TMD islands, and is thus suitable for the fabrication of large scale TMD/TMD heterostructures with highly controlled interlayer twist angle [46] to be embedded in microcavities. Together with additional hBN and graphene layers these structures could provide a viable route to realization of highly tunable and nonlinear dipolar polaritons [47] in large scale devices.

This work demonstrates the possibility to fabricate large scale polaritonic devices based on TMD-based heterostructures. Further development of large scale monolayer semiconductor growth techniques, most notably directly onto hBN which provides highly co-orientated TMD domains, will inevitably lead to heterostructures that can reliably and repeatedly compete with, or out-perform, those built with exfoliated flakes due to the unprecedented scalability that is granted.

4. Methods

4.1. Dielectric mirror fabrication

Highly reflecting distributed Bragg reflectors (DBRs) are deposited on silica substrates by ion beam sputtering. The DBRs are comprised of 13 pairs of quarter wavelength SiO_2/Ta_2O_5 layers, terminating with SiO_2, of thicknesses 129 and 89 nm (refractive index 1.45 and 2.10, respectively). The DBRs are designed for a center wavelength of 750 nm and a stop-band width of 200 nm.

Using focused Gallium ion beam milling into a planar fused silica substrate, the concave shaped template for the top mirror is formed [48]. The nominal radius of curvature of the concave mirror was 20 μm, prompting a beam waist of around 1 μm [8, 43] on the focal plane.

4.2. Growth of single layer $MoSe_2$ on c-plane sapphire

MoO_3 (99.97%, Sigma Aldrich) and Se (99.999%, Alfa Aesar) were used as precursors for the growth. 60 mg of MoO_3 powder was placed in the center of the furnace and 150 mg of Se was placed at the upstream entry. To minimize the intense evaporation of the MoO_3, the crucible that contained the precursor was partially covered by a SiO_2/Si wafer. The target substrate of c-plane sapphire was placed beside the crucible containing MoO_3.

The tube furnace was evacuated for 30 min and subsequently repleted with the Ar gas. Ambient pressure is reached before the furnace was heated to 600 $^{\circ}$C for 18 minutes under a steady flow of Ar gas (60 sccm) and H_2 gas (12 sccm). As the furnace temperature reached 600 $^{\circ}$C, the upstream entry of the tube was heated to 270 $^{\circ}$C, using a heating belt, as to vaporize Se. Finally, the furnace temperature was raised to 700 $^{\circ}$C, and maintained for 1 hour to facilitate the $MoSe_2$ growth. Upon completion, the tube furnace was cooled to room temperature whilst maintaining Ar flow, without H_2. Polystyrene was used to transfer $MoSe_2$ on top of the DBR in order to maintain sample quality.

4.3. Growth of single layer WSe_2 directly on hBN

Initially, hBN was grown on c-plane sapphire (see Methods). WO_3 (99.998%, Alfa Aesar) and Se (99.999%, Alfa Aesar) were used as precursors for the growth of single layer WSe_2. 120 mg of WO_3 powder, mixed with a small amount of NaCl to reduce the influence of humidity, was placed in the center of the furnace and 300 mg of Se was placed at the upstream entry. The target substrate of multilayer hBN on sapphire was placed beside the crucible that contained WO_3. The tube furnace was evacuated for more than 30 min before being heated to 800 $^{\circ}$C for 24 minutes under a steady flow of Ar gas (120 sccm) and H_2 gas (20 sccm). As the furnace temperature reached 800 $^{\circ}$C, the upstream entry of the tube was heated to 270 $^{\circ}$C, using a heating belt, as to vaporize Se. Finally, the furnace temperature was raised to, and maintained at, 870 $^{\circ}$C for 1 hour to facilitate WSe_2 growth. Upon completion, the tube furnace was cooled to room temperature whilst maintaining Ar flow, without H_2. In order to maintain sample quality, polystyrene was used to transfer the WSe_2/hBN stack to the DBR.

4.4. Growth of large area hBN

Multilayer hBN with an AA' stacking order was grown by remote inductively coupled plasma chemical vapor deposition method. A 2-inch c-plane sapphire was used as a substrate for the hBN growth. The substrate was placed in the center of a 2-inch alumina tube furnace of CVD. A borazine (Gelest, Inc.) precursor flask was placed in a water bath at -15 $^{\circ}$C. The bath temperature before the growth of hBN was

increased up to 25 °C. Before the growth of multilayer hBN, the furnace was heated to 1220 °C under flow of Ar gas (10 sccm). Plasma was generated at a power of 30 W under a flow of borazine (0.2 sccm) and Ar (10 sccm) gases for 30 mins. Atomic force microscopy and transmission electron microscopy measurements confirmed that the thickness of hBN was 1.2 nm, approximately 3 layers. In addition, the hBN sample shows quite good thickness uniformity over the 2-inch sapphire substrate according to the Raman and UV absorption spectra measured at nine random points over the 2-inch hBN film.

4.5. Optical measurements

The photoluminescence images of the CVD samples were acquired using a color camera (DS-Vi1, Nikon) equipped to a modified bright-field microscope (LV150N, Nikon). A 550 nm short-pass filter (FESH0550, Thorlabs) blocked the near-infrared emission from the white-light source, and a 600 nm long-pass filter (FELH0600, Thorlabs) was used to isolate the photoluminescence signal from the samples. A fully detailed description is available in Ref [49].

Spectrally-resolved photoluminescence and reflectance contrast measurements were implemented using a custom-built micro-PL setup. For photoluminescence, the samples were excited using two diode-pumped solid-state lasers (CW532-050 and ADL-66505TL, Roithner), centered at 2.33 eV and 1.88 eV. For reflectivity, a stabilized tungsten-halogen white-light source (SLS201L, Thorlabs) was used. A 50x objective lens (M Plan Apo 50X, Mitutoyo) was used to focus the excitation light onto the sample. A 0.5 m spectrometer (SP-2-500i, Princeton Instruments) with a nitrogen-cooled charge-coupled device camera (PyLoN:100BR, Princeton Instruments) is used to detect the signal from the samples, collected in the backwards direction. 700 nm and 650 nm long-pass filters (FEL0700 and FEL0650, Thorlabs) is used to isolate the PL signal. The reflectivity spectra were determined by comparing the collected white-light reflected from the DBR substrate and the sample, as $\Delta R/R = (R_{sub} - R_{HS})/R_{sub}$, where R_{HS} (R_{sub}) is the intensity of acquired light reflected by the sample (substrate).

Room-temperature measurements were carried out in ambient conditions. A continuous-flow liquid helium cryostat with a cold finger at a base temperature of ~5 K was employed to obtain the low-temperature measurements.

4.6. Tunable micro-cavity

The optical cavity was formed using an external concave mirror, with nominal radius of 20 μm, to produce a 0D tunable cavity [43].

The bottom mirror is controlled by a 5-axis piezo-actuator stack, the first three stages control the x, y, and z translational motion, while another two stages control the tilt alignment. The top mirror is positioned using a 3-axis piezo-actuator stage controlling the x, y, and z translational motion. Optical PL scans were completed with the samples placed in a helium bath cryostat system at a temperature of 4.2 K using a 637 nm continuous-wave laser diode (Vortran Stradus), focused onto the sample using an achromatic lens. The collected PL is focused onto a single mode fiber and guided into a 0.75 m spectrometer (SP-2-750i, Princeton Instruments) and a high-sensitivity charge-coupled device (PyLoN:400BR, Princeton Instruments) for emission collection.

4.7. Measurement of monolithic cavities

We performed the Fourier space spectral imaging of the PL emitted by the monolithic cavity by employing a 2D CCD array (PyLoN:100BR, Princeton Instruments) coupled to a 300 gr/mm grating spectrometer (SP-2-500i, Princeton Instruments). We focused a 30 cm lens onto the back plane of a 50x Mitutoyo infinity corrected objective to obtain the Fourier plane image of the sample, which was then projected on the slit of the spectrometer by using a 10 cm lens. We used the slit to select only the section of the Fourier space at $k_x = 0$, resulting in a final image on the CCD displaying the PL as a function of k_y on the y-axis and energy on the x-axis. The conversion from k_y to angles has been carried out by considering $k_y \approx \sin\theta$ and knowing that the maximum k_y detected by our setup is equal to the objective NA = 0.55

4.8. Flake orientation analysis

Optical microscope PL images were analyzed in MATLAB using the image processing toolbox functions [50]. A color thresholding application was used to visually separate monolayer material in a typical PL image. This thresholding is applied to all images analyzed by the shape recognition program. The program identified 8089 objects in HS1 and 8391 objects in HS2. A complete explanation of the analysis and further information regarding the image processing can be found in Ref [30].

4.9. Fabrication of monolithic cavities

The monolithic cavity has been fabricated by depositing a SiO_2 film of 98 nm on top of the CVD-grown monolayers, which were previously transferred on a 13 pairs SiO_2/Ta_2O_5 DBR grown by ion beam assisted sputtering on a sapphire substrate. In order to minimize the potential damages on the monolayers, the silica layer covering the TMDs has been grown at room temperature by using an e-beam deposition system. For the top mirror, a semi-transparent layer of Au (thickness: 50 nm) has been thermally evaporated, completing the cavity.

Acknowledgments

D J G, A G, T S M, and A I T acknowledge funding by EPSRC (EP/P026850/1 and EP/S030751/1). This work was supported by the research funds (NRF-2019R1A4A1027934 and NRF-2017R1E1A1A01074493) through National Research Foundation by the Ministry of Science and ICT, Korea. R J, K G, and D G L thank the financial support of EPSRC via programme grant 'Hybrid Polaritonics' (EP/M025330/1). T P L acknowledges financial support from the EPSRC Doctoral Prize Fellowship scheme Grant Reference EP/R513313/1. A I T thanks the financial support of the Graphene Flagship under grant agreements 785219 and 881603.

Data availability statement

The data that support the plots within this paper and other findings of this study are available from the corresponding author upon reasonable request.

Author contributions

D J G, A G, and S A contributed equally to this work. D J G, A G, T P L and T S M carried out optical investigations. TMD monolayers were grown via CVD and samples fabricated by S A and H S S. hBN layers were grown via CVD by K Y M and A-R J. The monolithic cavity was completed by R J, K G, and D G L. The concave mirrors were made by A A P T and J M S. Data was analyzed by D J G and A G. The manuscript was written by D J G with major input from A G and further contributions from all co-authors. A I T provided management of various aspects of the project, and contributed to the analysis and interpretation of the data and writing of the manuscript. A I T, H S S, D G L and J M S provided management of relevant parts of the project. A I T conceived and oversaw the whole project.

Competing interests

The authors declare no competing interests.

ORCID iDs

Daniel J Gillard https://orcid.org/0000-0002-0001-4918
Armando Genco https://orcid.org/0000-0002-1292-2614
Thomas P Lyons https://orcid.org/0000-0001-5569-7851
Aurélien A P Trichet https://orcid.org/0000-0002-0114-3340
Alexander I Tartakovskii https://orcid.org/0000-0002-4169-5510

References

[1] Novoselov K S, Jiang D, Schedin F, Booth T J, Khotkevich V V, Morozov S V and Geim A K 2005 Two-dimensional atomic crystals *Proc. Natl Acad. Sci. USA* **102** 10451–3
[2] Mak K F and Shan J 2016 Photonics and optoelectronics of 2D semiconductor transition metal dichalcogenides *Nat. Photon.* **10** 216–26
[3] Mak K F, He K, Lee C, Lee G H, Hone J, Heinz T F and Shan J 2013 Tightly bound trions in monolayer MoS 2 *Nat. Mater.* **12** 207–11
[4] He K, Kumar N, Zhao L, Wang Z, Mak K F, Zhao H and Shan J 2014 Tightly bound excitons in monolayer WSe2 *Phys. Rev. Lett.* **113** 1–5
[5] Xu X, Yao W, Xiao D and Heinz T F 2014 Spin and pseudospins in layered transition metal dichalcogenides *Nat. Phys.* **10** 343–50
[6] Liu X, Galfsky T, Sun Z, Xia F, Lin E-c, Lee Y-H, Kéna-Cohen S and Menon V M 2014 Strong light–matter coupling in two-dimensional atomic crystals *Nat. Photon.* **9** 30–4
[7] Dhara S, Chakraborty C, Goodfellow K M, Qiu L, O'Loughlin T A, Wicks G W, Bhattacharjee S and Vamivakas A N 2018 Anomalous dispersion of microcavity trion-polaritons *Nat. Phys.* **14** 130–3
[8] Dufferwiel S *et al* 2015 Exciton-polaritons in van der Waals heterostructures embedded in tunable microcavities *Nat. Commun.* **6** 1–7
[9] Sidler M, Back P, Cotlet O, Srivastava A, Fink T, Kroner M, Demler E and Imamoglu A 2017 Fermi polaron-polaritons in charge-tunable atomically thin semiconductors *Nat. Phys.* **13** 255–61
[10] Low T *et al* 2017 Polaritons in layered two-dimensional materials *Nat. Mater.* **16** 182–94
[11] Schneider C, Glazov M M, Korn T, Höfling S and Urbaszek B 2018 Two-dimensional semiconductors in the regime of strong light-matter coupling *Nat. Commun.* **9** 2695
[12] Krol M *et al* 2020 Exciton-polaritons in multilayer WSe_2 in a planar microcavity *2D Mater.* **7** 15006
[13] Dufferwiel S *et al* 2017 Valley-addressable polaritons in atomically thin semiconductors *Nat. Photon.* **11** 497–501
[14] Chen Y-J, Cain J D, Stanev T K, Dravid V P and Stern N P 2017 Valley-polarized exciton–polaritons in a monolayer semiconductor *Nat. Photon.* **11** 431–5
[15] Dufferwiel S *et al* 2018 Valley coherent exciton-polaritons in a monolayer semiconductor *Nat. Commun.* **9** 4797
[16] Qiu L, Chakraborty C, Dhara S and Vamivakas A N 2019 Room-temperature valley coherence in a polaritonic system *Nat. Commun.* **10** 1513
[17] Barachati F *et al* 2018 Interacting polariton fluids in a monolayer of tungsten disulfide *Nat. Nanotechnol.* **13** 906–9
[18] Lundt N *et al* 2019 Optical valley Hall effect for highly valley-coherent exciton-polaritons in an atomically thin semiconductor *Nat. Nanotechnol.* **14** 770–5
[19] Waldherr M *et al* 2018 Observation of bosonic condensation in a hybrid monolayer MoSe2-GaAs microcavity *Nat. Commun.* **9** 3286
[20] Emmanuele R P A *et al* 2020 Highly nonlinear trion-polaritons in a monolayer semiconductor *Nat. Commun.* **11** 3589
[21] Kasprzak J *et al* 2006 Bose-Einstein condensation of exciton polaritons *Nature* **443** 409–14
[22] Christopoulos S *et al* 2007 Room-temperature polariton lasing in semiconductor microcavities *Phys. Rev. Lett.* **98** 126405
[23] Bhattacharya P, Frost T, Deshpande S, Baten M Z, Hazari A and Das A 2014 Room temperature electrically injected polariton laser *Phys. Rev. Lett.* **112** 236802
[24] Amo A, Lefrère J, Pigeon S, Adrados C, Ciuti C, Carusotto I, Houdré R, Giacobino E and Bramati A 2009 Superfluidity of

polaritons in semiconductor microcavities *Nat. Phys.* **5** 805–10
[25] Liew T C H, Kavokin A V, Ostatnický T, Kaliteevski M, Shelykh I A and Abram R A 2010 Exciton-polariton integrated circuits *Phys. Rev.* B **82** 33302
[26] Ballarini D, De Giorgi M, Cancellieri E, Houdré R, Giacobino E, Cingolani R, Bramati A, Gigli G and Sanvitto D 2013 All-optical polariton transistor *Nat. Commun.* **4** 1778
[27] Shree S *et al* 2019 High optical quality of MoS 2 monolayers grown by chemical vapor deposition *2D Mater.* **7** 15011
[28] Zhang Y, Yao Y, Sendeku M G, Yin L, Zhan X, Wang F, Wang Z and He J 2019 Recent progress in CVD growth of 2D transition metal dichalcogenides and related heterostructures *Adv. Mater.* **31** 1901694
[29] Gebhardt C *et al* 2019 Polariton hyperspectral imaging of two-dimensional semiconductor crystals *Sci. Rep.* **9** 13756
[30] Severs Millard T, Genco A, Alexeev E M, Randerson S, Ahn S, Jang A-R, Shin H S and Tartakovskii A I 2020 Large area chemical vapour deposition grown transition metal dichalcogenide monolayers automatically characterized through photoluminescence imaging *Npj 2D Mater. Appl.* **4** 12
[31] Ajayi O A *et al* 2017 Approaching the intrinsic photoluminescence linewidth in transition metal dichalcogenide monolayers *2D Mater.* **4** 031011
[32] Del Pozo-Zamudio O *et al* 2020 Electrically pumped WSe_2-based light-emitting van der Waals heterostructures embedded in monolithic dielectric microcavities *2D Mater.* **7** 31006
[33] Zhang X *et al* 2019 Defect-controlled nucleation and orientation of WSe 2 on hBN: A route to single-crystal epitaxial monolayers *ACS Nano* **13** 3341–52
[34] Okada M, Sawazaki T, Watanabe K, Taniguch T, Hibino H, Shinohara H and Kitaura R 2014 Direct chemical vapor deposition growth of WS2 atomic layers on hexagonal boron nitride *ACS Nano* **8** 8273–7
[35] Yu H *et al* 2017 Precisely aligned monolayer MoS 2 epitaxially grown on h-BN basal plane *Small* **13** 1603005
[36] Ross J S *et al* 2013 Electrical control of neutral and charged excitons in a monolayer semiconductor *Nat. Commun.* **4** 1473–6
[37] Robert C *et al* 2017 Fine structure and lifetime of dark excitons in transition metal dichalcogenide monolayers *Phys. Rev.* B **96** 155423
[38] Lindlau J *et al* 2018 The role of momentum-dark excitons in the elementary optical response of bilayer WSe2 *Nat. Commun.* **9** 2586
[39] Jadczak J, Kutrowska-Girzycka J, Kapuściński P, Huang Y S, Wójs A and Bryja L 2017 Probing of free and localized excitons and trions in atomically thin WSe 2, WS 2, MoSe 2 and MoS 2 in photoluminescence and reflectivity experiments *Nanotechnology* **28** 395702
[40] Lippert S *et al* 2017 Influence of the substrate material on the optical properties of tungsten diselenide monolayers *2D Mater.* **4** 025045
[41] Dumcenco D *et al* 2015 Large-area epitaxial monolayer MoS 2 *ACS Nano* **9** 4611–20
[42] Zhang X *et al* 2018 Diffusion-controlled epitaxy of large area coalesced WSe 2 monolayers on sapphire *Nano Lett.* **18** 1049–56
[43] Schwarz S *et al* 2014 Two-dimensional metal-chalcogenide films in tunable optical microcavities *Nano Lett.* **14** 7003–8
[44] Kavokin A, Baumberg J J, Malpuech G and Laussy F P 2007 *Microcavities* (Oxford: Oxford University Press) pp 1–432
[45] Genco A, Giordano G, Carallo S, Accorsi G, Duan Y, Gambino S and Mazzeo M 2018 High quality factor microcavity OLED employing metal-free electrically active Bragg mirrors *Org. Electron.* **62** 174–80
[46] Alexeev E M *et al* 2019 Resonantly hybridized excitons in moiré superlattices in van der Waals heterostructures *Nature* **567** 81–6
[47] Cristofolini P, Christmann G, Tsintzos S I, Deligeorgis G, Konstantinidis G, Hatzopoulos Z, Savvidis P G and Baumberg J J 2012 Coupling quantum tunneling with cavity photons *Science* **336** 704–7
[48] Dolan P R, Hughes G M, Grazioso F, Patton B R and Smith J M 2010 Femtoliter tunable optical cavity arrays *Opt. Lett.* **35** 3556
[49] Alexeev E M *et al* 2017 Imaging of interlayer coupling in van der waals heterostructures using a bright-field optical microscope *Nano Lett.* **17** 5342–9
[50] MathWorks 2017 *Image Processing Toolbox User's Guide* 195-207